



# Power Spectra of Random Heterogeneities of the Solid Earth

Haruo Sato<sup>1</sup>

<sup>1</sup>Geophysics, Science, Tohoku University, Aoba-ku, Sendai-shi, Miyagi-ken, 980-8578, Japan

**Correspondence:** Haruo Sato (haruo.sato.e2@tohoku.ac.jp)

**Abstract.** Recent seismological observations focusing on the collapse of an impulsive wavelet revealed the existence of small-scale random heterogeneities in the earth medium. The radiative transfer theory (RTT) is often used for the study of the propagation and scattering of wavelet intensities, the mean square amplitude envelopes. For the statistical characterization of the power spectral density function (PSDF) of the random fractional fluctuation of velocity inhomogeneities in a 3D space, we use von Kármán type with three parameters: the root mean square (RMS) fractional velocity fluctuation, the characteristic length, and the order of the modified Bessel function of the second kind, which leads to the power-law decay of PSDF at wavenumbers higher than the corner. We compile reported statistical parameters of the lithosphere and the mantle based on various types of measurements for a wide range of wavenumbers: photo scan data of rock samples, acoustic well log data, and envelope analyses of cross-hole experiment seismograms, regional seismograms and tele-seismic waves based on the RTT. Reported exponents of wavenumber are distributed between  $-3$  and  $-4$ , where many of them are close to  $-3$ . Reported RMS fractional fluctuations are of the order of  $0.01 \sim 0.1$  in the crust and the upper mantle. Reported characteristic lengths distribute very widely, however, each one seems to be restricted by the dimension of the measurement system or the sample length. In order to grasp the spectral characteristics, eliminating strong heterogeneity data and the lower mantle data, we have plotted all the reported PSDFs of the crust and the upper mantle against wavenumber for a wide range  $10^{-3} \sim 10^8 \text{ km}^{-1}$ . We find that the envelope of those PSDFs is well approximated by the  $-3$ rd power of wavenumber. It suggests that the earth medium randomness has a broad spectrum. In theory, we need to re-examine the applicable range of the Born approximation in the RTT when the wavenumber of a wavelet is much higher than the corner. In observation, we will have to measure carefully the PSDF on both sides of the corner. We may consider the obtained power-law decay spectral envelope as a reference for studying the regional differences. It is interesting to study what kinds of geophysical processes created the observed power-law spectral envelope in different scales and in different portions of the solid earth medium.

*Copyright statement.* TEXT

## 1 Introduction

The first image of the solid earth is composed of spherical shells, for example, PREM. As seismic networks were deployed on the regional scale and worldwide, the velocity tomography based on the ray tracing method revealed 3D heterogeneous



structure in various scales; however, spatial variations of resultant velocity structures are essentially smooth compared with seismic wavelengths. Aki and Chouet (1975) first put a focus on long lasting coda waves of small earthquakes and interpreted them as scattered waves by small-scale random heterogeneities. They proposed to measure the scattering coefficient  $g$ , the scattering power per unit volume as a measure of medium heterogeneity. They analyzed the mean square (MS) amplitude time trace of coda waves as an incoherent sum of scattered waves' power by using the Born approximation (e.g. Chernov, 1960), which is a simplified version of the radiative transfer theory (RTT). There have been many measurements of the total scattering coefficient  $g_0$  supposing isotropic scattering (e.g. Sato, 1977a) in various seismo-tectonic environments. The total scattering coefficient, the reciprocal of the mean free path of S-waves is reported to be of the order of  $10^{-2} \text{ km}^{-1}$  for  $1 \sim 20 \text{ Hz}$  in the lithosphere, and it marks a higher value beneath active volcanoes (e.g. Sato et al., 2012; Yoshimoto and Jin, 2008). There were precise measurements of regional variations in  $g_0$  as Carcolé and Sato (2010) in Japan and Eulenfeld and Wegler (2017) in US. Hock et al. (2004) analyzed medium heterogeneity in Europe from the analyses of tele-seismic waves using the modified energy flux model (Korn, 1993). There were also measurements of the anisotropic scattering coefficient from the analysis of S coda envelopes (e.g. Jing et al., 2014; Zeng, 2017).

Aki and Chouet (1975) derived the angular dependence of the scattering coefficient of scalar waves from the power spectral density function (PSDF) of the fractional velocity fluctuation using the Born approximation. Sato (1984) extended the envelope synthesis of scalar waves to the the whole envelope synthesis of 3-component seismograms from the P onset to S coda on the bases of the single scattering approximation of the RTT. His syntheses well explains how seismogram envelopes in different back azimuths vary depending on the source fault mechanism. Extension to the multiple scattering case was developed by using Stokes parameters (e.g. Margerin et al., 2000; Margerin, 2005; Przybilla et al., 2009). We also note that the Monte Carlo simulation was developed to solve stochastically the RTT (e.g. Hoshiya et al., 1991; Gusev and Abubakirov, 1987; Yoshimoto, 2000). For the data processing, it is more appropriate to stack MS envelopes of observed seismograms for comparison with the averaged intensity time traces stochastically synthesized by the RTT (e.g. Shearer and Earle, 2004; Rost et al., 2006; da Silva et al., 2018).

As the center wavenumber of a wavelet increases much larger than the corner wavenumber of the PSDF, the wavelet around the peak value is mostly composed of narrow angle scattering around the forward direction. In such a case, the Born approximation becomes inappropriate; however, the phase shift modulation based on the parabolic approximation is useful, which is called the phase screen approximation. As an extension of the RTT with the phase screen approximation, the Markov approximation was also used for the analysis of envelope broadening and peak delay with increasing travel distance (e.g. Sato, 1989; Saito et al., 2002; Takahashi et al., 2009). Kubanza et al. (2007) measured regional differences in the lithospheric heterogeneity from the partitioning of seismic energy of tele-seismic P waves into the vertical and transverse components based on the Markov approximation.

There have been various kinds of measurements of the PSDF of the random velocity fluctuation, where the PSDF is often supposed to be von Kármán type. In the following section, the main objective of this paper is to compile reported PSDF measurements in various scales in different portions of the solid earth: photo scanning of small rock samples, acoustic well logs, array analyses of tele-seismic waves; waveform analyses using FD simulations, analyses of seismogram envelopes on the

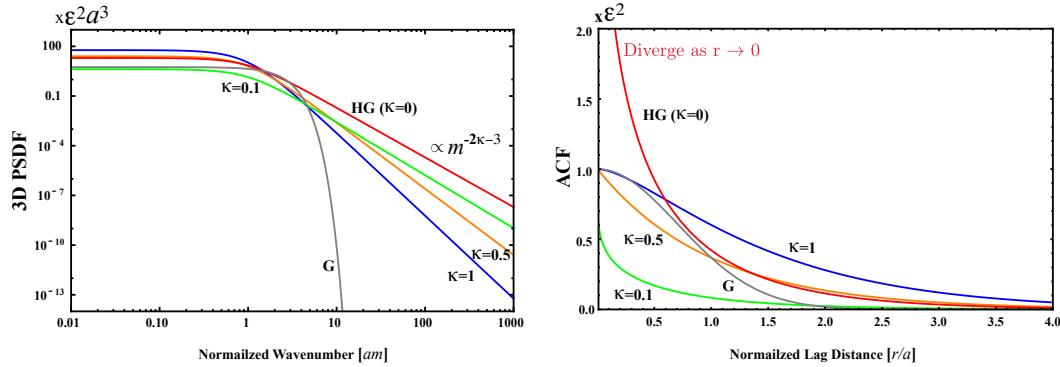


**Figure 1.** (a) Log-log plot of PSDF vs. wavenumber  $m$  in 3-D space (von Kármán-type,  $\kappa=0.1, 0.5$  and 1; Henyey-Greenstein type, HG,  $\kappa=0$ ; Gaussian type, G). (b) Linear plot of ACF vs. lag distance  $r$ . The ordinate is normalized by  $a$ .

basis of the RTT. We enumerate their statistical parameters and plot their PSDFs against wavenumber. We will show that the envelope of all the PSDFs is well approximated by a power-law decay curve. Then, we will discuss the results obtained and a few problems in the envelope synthesis theory for such random media and the geophysical origin of such power spectra.

## 2 Statistical characterization of random media

- 5 We consider the propagation of scalar waves as a simple model, where the inhomogeneous velocity is given by  $V(\mathbf{x}) = V_0(1 + \xi(\mathbf{x}))$ . The fractional fluctuation  $\xi(\mathbf{x})$  is a random function of space. We imagine an ensemble of random media  $\{\xi(\mathbf{x})\}$ , where  $\langle \xi \rangle = 0$ . Angular brackets mean the ensemble average. We suppose that random media are homogeneous and isotropic, then we statistically characterized them by using the auto-correlation function (ACF):

$$R(\mathbf{x}) = R(r) = \langle \xi(\mathbf{y})\xi(\mathbf{y} + \mathbf{x}) \rangle, \quad (1a)$$

- 10 where  $r = |\mathbf{x}|$ . The MS fractional fluctuation as a measure of the strength of randomness is supposed to be small,  $\varepsilon^2 \equiv R(0) \ll 1$ . The Fourier transform of ACF gives the PSDF<sup>1</sup> :

$$P(\mathbf{m}) = P(m) = \iiint_{-\infty}^{\infty} R(\mathbf{x}) e^{-i\mathbf{m}\mathbf{x}} d\mathbf{x}, \quad (1b)$$

where wavenumber  $m = |\mathbf{m}|$ .



## 2.1 Several types of random media

There are several types of PSDF and ACF characterized by a few parameters.

### von Kármán-type

The ACF is written by using a modified Bessel function of the second kind of order  $\kappa$  and characteristic length  $a$ :

$$5 \quad R(r) = \frac{2^{1-\kappa}}{\Gamma(\kappa)} \varepsilon^2 \left(\frac{r}{a}\right)^\kappa K_\kappa\left(\frac{r}{a}\right) \quad \text{for } \kappa > 0, \quad (2a)$$

which is an exponential type  $R(r) = \varepsilon^2 e^{-r/a}$  when  $\kappa = 1/2$ . In the case of space dimension  $d$ , the PSDF is

$$P(m) = \frac{2^d \pi^{\frac{d}{2}} \Gamma(\kappa + \frac{d}{2}) \varepsilon^2 a^d}{\Gamma(\kappa) (1 + a^2 m^2)^{\kappa + \frac{d}{2}}} \quad \text{for } \kappa > 0$$

$$\propto m^{-2\kappa-d} \quad \text{for } m \gg a^{-1}. \quad (2b)$$

The PSDF obeys a power-law decay at large wavenumbers:  $P(m) \propto m^{-2\kappa-3}$  for the 3D case and  $P(m) \propto m^{-2\kappa-1}$  for the  
 10 1D case, where  $\kappa$  corresponds to the Hurst number. In the following we will basically use von Kármán-type for characterizing the earth medium heterogeneity. Especially for an anisotropic case, we define the PSDF of von Kármán-type in 3D (e.g. Wu et al., 1994; Nakata and Beroza, 2015):

$$15 \quad P(m) = \frac{2^d \pi^{\frac{d}{2}} \Gamma(\kappa + \frac{3}{2}) \varepsilon^2 a_x a_y a_z}{\Gamma(\kappa) (1 + a_x^2 m_x^2 + a_y^2 m_y^2 + a_z^2 m_z^2)^{\kappa + \frac{3}{2}}} \quad \text{for } \kappa > 0. \quad (3)$$

### 15 Henyey-Greenstein type

For a case formally corresponding to  $\kappa = 0$  of von Kármán-type, we define Henyey-Greenstein type in 3D (Henyey and Greenstein, 1941):

$$R(r) = \varepsilon^2 K_0\left(\frac{r}{a}\right), \quad (4a)$$

$$20 \quad P(m) = \frac{2\pi^2 \varepsilon^2 a^3}{(1 + a^2 m^2)^{3/2}} \approx 2\pi^2 \varepsilon^2 m^{-3} \quad \text{for } m \gg a^{-1}. \quad (4b)$$

Note that parameter  $\varepsilon^2$  characterizes  $P$  but  $\varepsilon^2 \neq R(0)$  since  $R(r)$  diverges as  $r \rightarrow 0$ .

### Gaussian-type

Gaussian-type is also used because it is mathematically tractable.

$$25 \quad R(r) = \varepsilon^2 e^{-\frac{r^2}{a^2}}, \quad (5a)$$

$$P(m) = \sqrt{\pi^3} \varepsilon^2 a^3 e^{-\frac{m^2 a^2}{4}}. \quad (5b)$$

We plot those PSDFs against wavenumber and ACFs against lag distance in Figure 1.

<sup>1</sup>In some literature,  $(2\pi)^{-3}$  is used as a prefactor in the righthand side of (1b).



### 3 Measurements of random heterogeneities

There are several kinds of measurements for estimating statistical parameters characterizing random media. Here we principally collect measurements supposing von Kármán type for isotropic randomness; however, we include a few measurements supposing Gaussian type. In a small scale, photo scan method is applied to small rock samples. Acoustic well logs are available in deep wells drilled in the shallow crust. When the precise velocity tomography result is available, we can directly calculate the PSDF. In seismology, the most conventional method is to analyze seismograms of natural earthquakes or artificial explosions after traveling through the earth heterogeneity. It is better to focus on MS amplitude envelopes since phases are complex caused by random heterogeneities. Comparing observed seismogram envelopes with synthesized envelopes, we can evaluate von Kármán parameters. For the synthesis, we can use the finite difference simulation (FD), the RTT with the Born approximation, and the RTT with the phase screen approximation that is equivalent to the Markov approximation. For each reported measurement, we enumerate the target region, data and method, measured PSDF as a function of wavenumber  $m$ , von Kármán parameters ( $\kappa$ ,  $\varepsilon$ ,  $a$ ), the frequency range, the wavenumber range, and reference in Tables 1~3. Especially in seismological measurements, we estimate the wave number range from the frequency range by using the typical velocity of the target medium. In Tables, the parameter value in brackets ( $\dots$ ) is fixed in the measurement. Then, we plot obtained PSDFs against wavenumber in Figures 2~4. When a parameter is given by a range, the parameter value in squared brackets [ $\dots$ ] is used as the representative value for plotting PSDFs in Figures. A measurement of label with an asterisk \* is not used for plotting since the parameter set is not complete.

#### 3.1 Photo scan of the rock surface

The photo scan method uses a scanner to take a picture of the polished flat surface of a small rock sample (e.g. Sivaji et al., 2002; Spetzler et al., 2002; Fukushima et al., 2003). For the case of a granite sample, they classified color images on a straight line into three types of mineral grains; quartz, plagioclase and biotite. Assigning a typical velocity  $V_P$  or  $V_S$  to each mineral grain, they constructed a velocity profile on the line. Then, they estimated the 1D PSDF of the velocity fractional fluctuation. They analyzed 1D PSDFs of granite and gabbro samples fixing von Kármán-type curve of  $\kappa=0.5$  as R1~R5. Figure 2 (a) shows estimated 1D PSDF, where the wavenumber range is of the order of  $1 \text{ mm}^{-1}$ . Figure 2 (b) shows corresponding 3D PSDFs. We note that raw 1D PSDFs in Figures 4 and 5 of Fukushima et al. (2003) decay a little slower than R4 and R5 in Figure 2 (a) especially at large wavenumbers.

#### 3.2 Acoustic well loggings in boreholes

An acoustic well log is obtained from the measurement of the travel time of an ultrasonic pulse along the wall of a well. Measurements W1 (volcanic tuff) and W2 (tertiary to pre-tertiary) in Japan clearly show power law decay with  $\kappa = 0.225$  and 0.045, respectively; however, a corner is not clearly seen in each PSDF. Measurement W4 at the deep well KTB in Germany shows  $\kappa=0.10$ . Measurement W3 in the same well shows that the exponent of wavenumber is  $-0.97$ , which formally corresponds to a negative  $\kappa$ . Measurement W5 at Cajon pass in California shows  $\kappa = 0.11$ . All these measurements show very

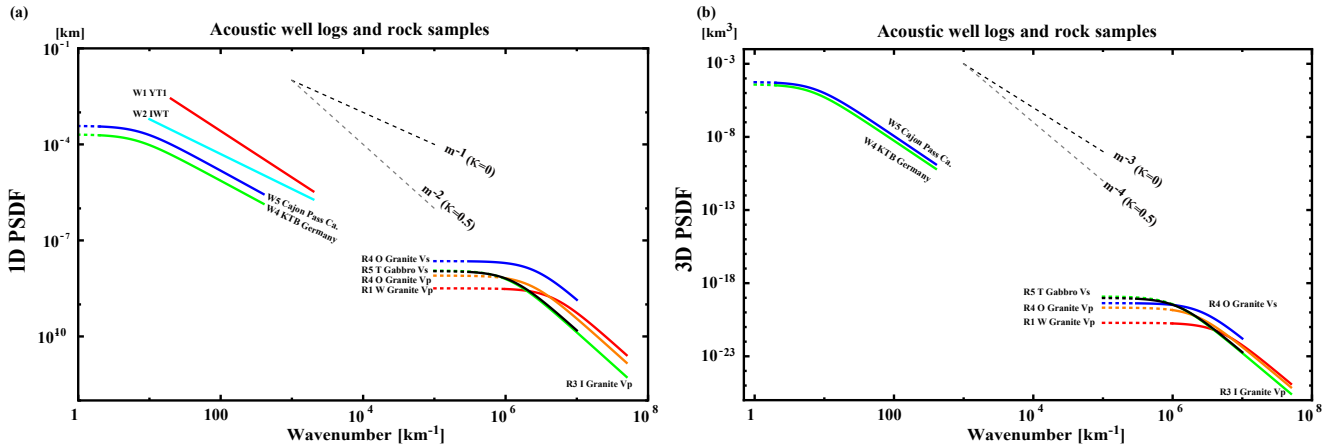


**Figure 2.** (a) 1D PSDF vs. wavenumber and (b) converted 3D PSDF vs. wavenumber for rock samples and acoustic well logs. See labels in Table 1.

small  $\kappa$  values close to 0. Measurement of  $a$  seems to be restricted by the sample length. We enumerate those measurements in Table 1 and plot their 1D PSDFs against wavenumber in Figure 2 (a). Figure 2 (b) shows plots the corresponding 3D PSDFs of W4 and W5. We note that Wu et al. (1994) measured anisotropy of randomness from the analysis of well-logs obtained from two parallel wells at KTB: the horizontal scale is larger than the vertical scale,  $a_h/a_z=1.8$  (see (3)) as shown in W3.

### 5 3.3 Velocity tomography

There have been measurements of velocity tomography in various scales, from which we can calculate the PSDF and then estimate von Kármán-type parameters. This method depends on the spacial resolution of tomography result. Measurement L1 in Table 2 is calculated from the precise  $V_P$  tomography result of the shallow crust, Los Angeles, California: the exponent of wavenumber is  $-3.08$  ( $\kappa = 0.04$ ). Anisotropic randomness is also reported:  $a_z=0.1$  km and  $a_h=0.5$  km (see eq. (3)). We show those in Figures 3. Measurement M2 in Table 3 shows the 2D PSDF of  $V_S$  tomography result of the upper mantle in a low wavenumber range; the exponent of wavenumber varies from  $-2$  to  $-3$ , which means  $0 < \kappa < 0.5$ . We note that Figure 8 of Mancinelli et al. (2016a) shows that the 1D PSDF estimated from the  $V_P$  tomography result in the upper mantle (Meschede and Romanowicz, 2015) well covers that of MU2 ( $\kappa=0.05$ ,  $\varepsilon=0.1$ ,  $a=2000$  km) for the wavenumber range  $2 \times 10^{-4} \sim 10^{-2}$  km $^{-1}$ .

### 3.4 Array analysis of tele-seismic P waves

15 Tele-seismic P waves registered by a large aperture array were used for the evaluation of 3D PSDF of the lithosphere beneath the array: LA1 and LA2 of Table 2 in Montana and LA3 in southern California used amplitude and phase coherence analyses, where Gaussian-type PSDF (eq. (5)) was supposed because of mathematical simplicity. As shown in Figure 3 (b), they drop very fast as wavenumber increases. Later Flatté and Wu (1988) developed the angular coherence analysis in addition to the above methods. Analyzing teleseismic P waves registered at NORSAR, they proposed a two overlapping layer model LA4, which is

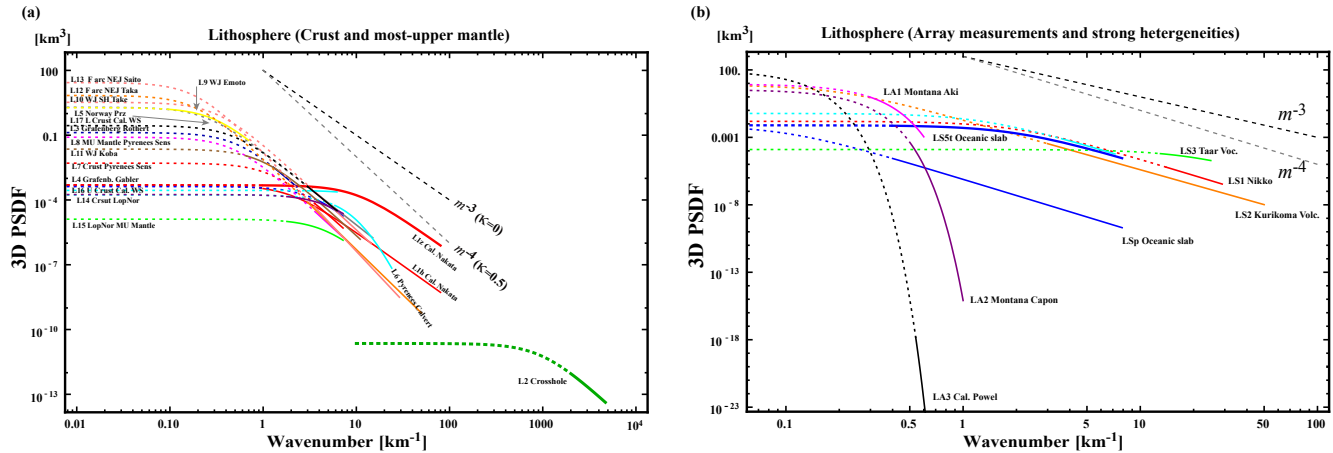


**Figure 3.** 3D PSDF vs. wavenumber for (a) the lithosphere (the crust and most upper mantle), (b) strong heterogeneities and array data analyses in the lithosphere. See labels in Table 2.

composed of a band-limited flat spectrum from the surface to 200 km in depth and  $m^{-4}$  spectrum ( $\kappa = 0.5$ ,  $\varepsilon = 1 \sim 4\%$ ) for depths from 15 to 250 km. It means  $\kappa < 0.5$  and the roll-off of their PSDF is much smaller than that of Gaussian types (not shown in Figure 3 (b)).

### 3.5 Finite difference simulations

- 5 The finite difference (FD) simulation is often used for the numerical simulation of waves in an inhomogeneous velocity structure. For the evaluation of average MS amplitude envelopes, we have to repeat simulations of the wave propagation through random media having the same PSDF that are generated by using different random seeds. There are several measurements of statistical parameters using FD as L9~L11 and ML4 in Tables 2 and 3. Measurement LS5 focused on the fact that the subducting oceanic plate is an efficient waveguide for high-frequency seismic waves: estimated anisotropic parameters are  $\kappa=0.5$ ,  $\varepsilon=0.02$ ,  $a_{\parallel}=10$  km,  $a_{\perp}=0.5$  km. Note ML2 supposes Gaussian-type.

### 3.6 Analyses of seismogram intensities (MS amplitude envelopes)

- The RTT is essentially stochastic to synthesize directly the intensity (the average MS amplitude envelope) of a wavelet propagating through random media. There are two conventional methods on the basis of the RTT: one uses the Born approximation and the other uses the phase screen approximation based on the parabolic approximation when the wavenumber is larger than the corner. The former neglects the phase shift, but the latter correctly considers the phase shift.

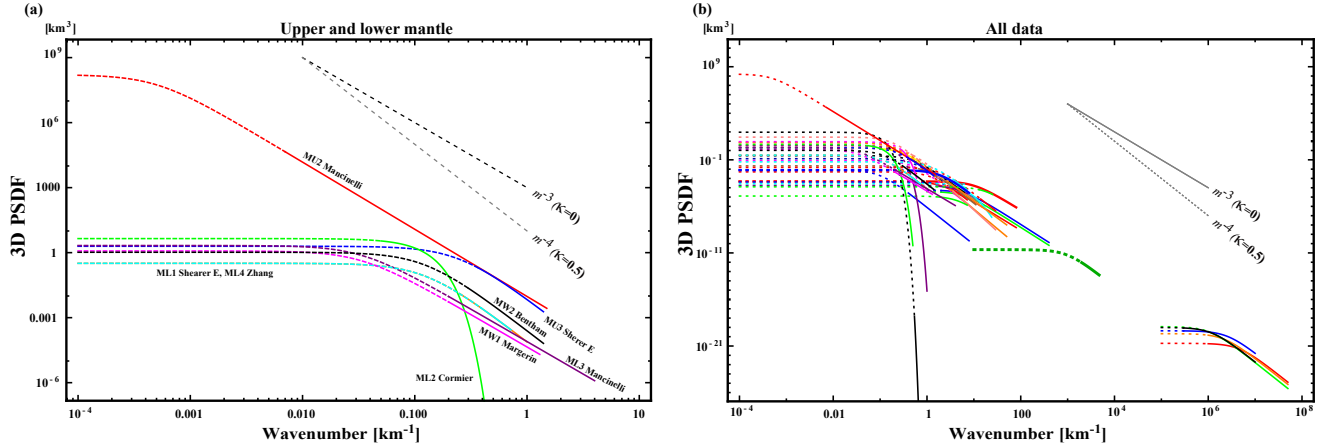


**Figure 4.** 3D PSDF vs. wavenumber for (a) the upper and lower mantle, and (b) all the data. See labels in Table 3.

### 3.6.1 Scalar wave scattering by a single obstacle

We here study the deterministic scattering of scalar waves by a single spherical obstacle (radius  $a = 5$  km and velocity anomaly  $\varepsilon = +0.05$ ) embedded in a homogeneous medium ( $V_0 = 4$  km/s) as a mathematical model. The Born approximation calculates spherically outgoing scattered waves putting the incident plane wave of wavenumber  $k_c$  in the interaction term of the first order perturbation equation. From the scattering amplitude we evaluate the total scattering cross-section  $\sigma_0$ . The resultant  $\sigma_0$  monotonously increases with frequency as shown by a blue line in Figure 5. As the wavenumber increases ( $ak_c \gg 1$ ), the phase shift increases as the incidence plane wave penetrates the obstacle. Putting the phase modulated wave according to the parabolic approximation (the phase screen approximation) into the interaction term of the first order perturbation equation, we calculate the scattering amplitude and then the total scattering cross-section. It is the distorted-wave Born approximation with the phase screen approximation, which is also referred to as the Eikonal approximation. This approximation predicts that  $\sigma_0$  (a red line in Figure 5) saturates at high frequencies and converges to  $2\pi a^2$ , which is twice the geometrical section area of the obstacle as predicted by shadow scattering (e.g. Landau and Lifshitz, 2003, p. 519 and 543). We recognize that the conventional Born approximation is still accurate even for  $ak_c > 1$ ; however, it works well only for  $\varepsilon^2 a^2 k_c^2 \lesssim O(0.1)$ . We should use the distorted-wave Born approximation with the phase screen approximation for  $\varepsilon^2 a^2 k_c^2 \gtrsim O(1)$ . Two approximations predict nearly the same  $\sigma_0$  value in the intermediate range. We note that  $2\varepsilon a k_c$  is the phase shift on the center line after passing the obstacle.

Interpreting  $\varepsilon$  and  $a$  as the RMS fractional fluctuation and the characteristic length of uniformly distributed random media, we may use the inequality  $\varepsilon^2 a^2 k_c^2 \ll O(1)$  or  $\varepsilon^2 a^2 k_c^2 \lesssim O(0.1)$  as a criterion of the Born approximation, which is the same as the criterion of the Bourret approximation (Rytov et al., 1989).

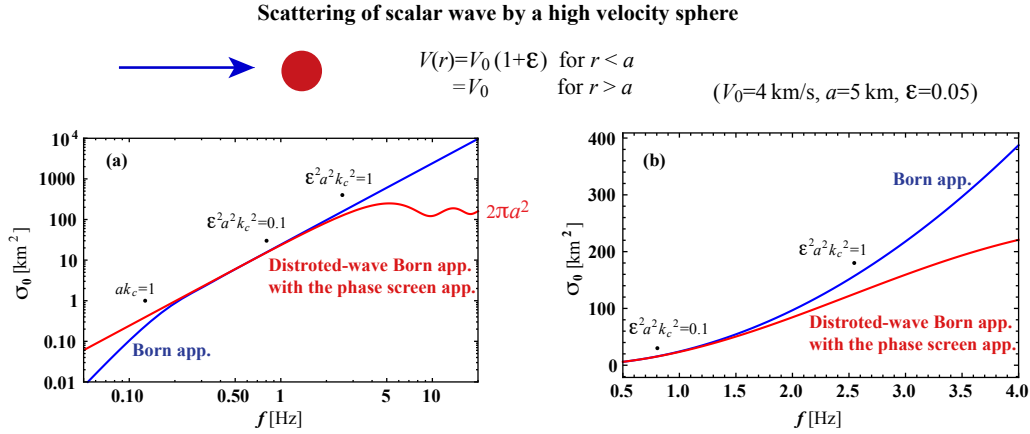


**Figure 5.** Scattering of scalar waves by a high velocity sphere. (a) Log-log plot of the scattering cross-section against frequency. (b) Semi log plot for zoom up. The Born approximation and the distorted-wave Born approximation with the phase screen approximation are drawn by blue and red lines, respectively.

### 3.6.2 RTT with the Born approximation

For uniformly distributed random media characterized by  $P(m)$ , the Born approximation leads to the scattering coefficient at the wavenumber  $k_c$  into scattering angle  $\psi$ :

$$g(k_c, \psi) = \frac{k_c^4}{\pi} P(2k_c \sin \frac{\psi}{2}). \quad (6a)$$

5 The total scattering coefficient, the reciprocal of the mean free path is

$$g_0(k_c) \equiv \frac{1}{4\pi} \oint g(k_c, \psi) d\Omega = \frac{1}{2} \int_0^\pi g(k_c, \psi) \sin \psi d\psi = \int_0^{2k_c} g_{ker}(k_c, m) dm, \quad (6b)$$

where  $m = 2k_c \sin \frac{\psi}{2}$ . The integral kernel in the wavenumber space is given by

$$g_{ker}(k_c, m) = \frac{k_c^2}{2\pi} m P(m). \quad (6c)$$

The upper bound of the integral is twice the wavenumber. As an example, Figure 6 shows plots of  $P(m)$  (blue) vs.  $m$  and  
 10  $g_{ker}(m)$  vs.  $m$  at 0.1 Hz (red) and 1 Hz (green) for the case of  $\kappa=0.5$ ,  $\epsilon=0.05$ ,  $a=1$  km and  $V_0=4$  km/s. As shown at the upper-right corner, the scattering pattern at 1 Hz has a large lobe into the forward direction; however, it becomes isotropic as the wavenumber decreases. Dots on each  $g_{ker}$  curve show corresponding scattering angles.

In the framework of the RTT, the Monte Carlo simulation is a simple method to synthesize stochastically the wavelet  
 intensity time trace. A particle carrying unit intensity is shot randomly from a point source, and its trajectory is traced with the  
 15 increment of time steps. The occurrence of scattering is stochastically tested by inequality  $g_0 V_0 \Delta t > \text{Random}[0,1]$  at every

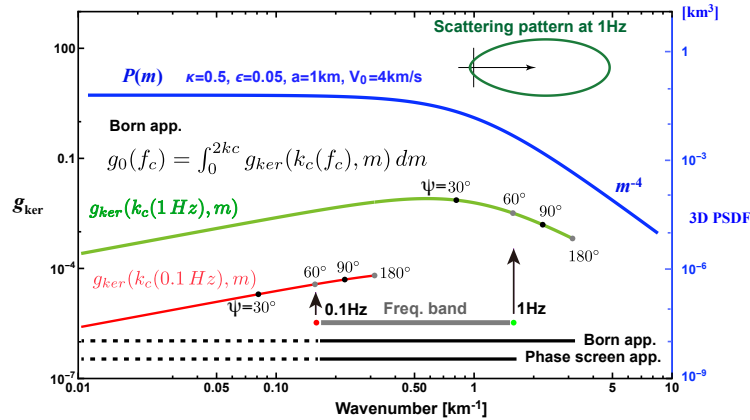


**Figure 6.** Plot of 3D PSDF  $P(m)$  (blue, right scale) and the spectral kernel of the scattering coefficient  $g_{ker}(k_c(f_c), m)$  at  $f_c=0.1$  Hz (red, left scale) and 1 Hz (green, left scale) according to the Born approximation. Scattering angles are marked by dots on each trace. For the case of frequency band between 0.1 and 1 Hz, the phase screen approximation based on the parabolic approximation covers the wavenumber range from 0 to the upper bound (line at the bottom), however, the Born approximation covers the range from 0 to twice the upper bound (line next to the bottom). We use those line styles in Figures 3~4 and 8.

time step of  $\Delta t$ , and  $g(k_c, \psi)/(4\pi g_0(k_c))$  is used as the probability of scattering into angle  $\psi$ . Note that  $\text{Random}[0,1]$  is a uniform random variable between 0 and 1. Since  $g_0 V_0 \Delta t$  is chosen to be small enough, scattering does not occur every time step but intermittently. As a simple example, Figure 7 (a) schematically illustrates the flowchart of the Monte Carlo simulation for the isotropic radiation from a point source in uniform random media. At lapse time  $t$ , dividing the number of particles  $n$  registered in a spherical shell of radius  $r$  and a thickness  $\Delta r$  by the total number of particles  $N$  and the shell volume  $4\pi r^2 \Delta r$ , we calculate the intensity Green function  $G(r, t)$ . The intensity time trace  $I(r, t)$  is calculated by the convolution of  $G(r, t)$  and the source intensity time function  $S(t)$  in the time domain. It is easy to introduce a layered structure of background velocity and intrinsic absorption into the simulation code.

The RTT for the scalar wave case can be extended to the elastic vector wave case by using Stokes parameters. There are four scattering modes, PP, PS, SS and SP scatterings, each of which is anisotropic (see Sato et al., 2012, Figure 4.7). Many papers (e.g. Shearer and Earle, 2004; Przybilla et al., 2009) suppose proportional relations  $\delta V_p/V_{P0} = \delta V_s/V_{S0} = \xi$  and  $\delta \rho/\rho_0 \propto \xi$  based on the empirical Birch's law, which reduce three fractional fluctuations into one (e.g. Sato et al., 2012, eqs. 4.58 and 4.59).

The RTT with the Born approximation has been often used not only for the analyses of S coda envelopes but also for the whole seismogram envelope from the P onset via P coda through S wave until S coda (see Tables 2 and 3). This method has been often used not only for the analyses of regional seismograms propagating through the lithosphere but also for the analyses of tele-seismic waves propagating through the mantle. This method is applied to analyze not only direct P phase but also PcP

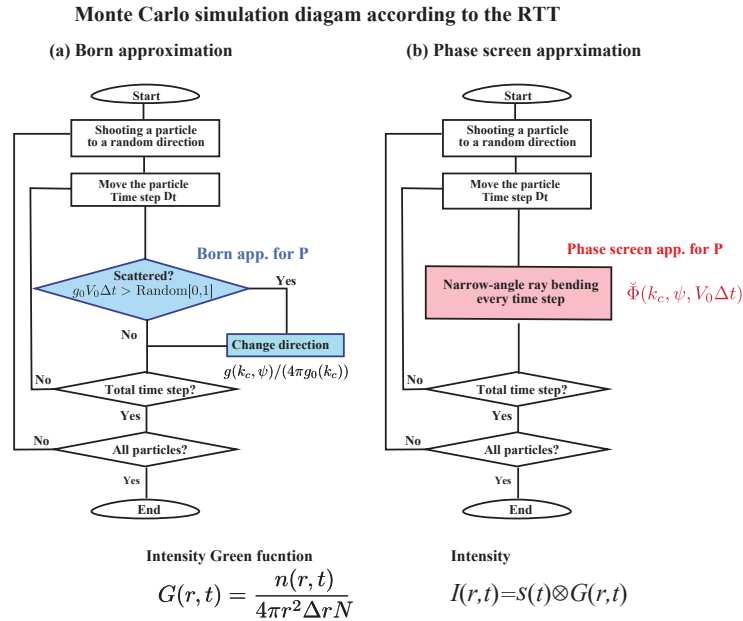


**Figure 7.** Flowchart of the Monte Carlo simulation code according to the RTT for the scalar wavelet intensity in uniform random media. (a) RTT with the Born approximation. (b) RTT with the phase screen approximation.

and PKP<sub>prec</sub> phases and so on. In this review, we discard intrinsic absorption parameters a priori assumed or measured in each paper since there are variations in methods. For a given wavenumber range ( $k_l, k_u$ ) (gray) in Figure 6, each PSDF curve using this method in Figures 3 and 4 is drawn by a dotted line for  $(0, k_l)$  and a solid line for  $(k_l, 2k_u)$  as the line next to the bottom of Figure 6. As indicated by dots on the  $g_{ker}$  curves, the wavenumber interval of solid line reflects wide angle scattering and that of dotted line reflects narrow angle scattering around the forward direction.

Most of measurements of S-waves in the lithosphere cover the wavenumber range up to  $100 \text{ km}^{-1}$ . Measurement L2 analyzed cross-hole seismograms of the order of kHz by using 2D-RTT, of which the wavenumber range is as high as the order of  $1 \text{ m}^{-1}$ . Measurement MU2 for tele-seismic P wave envelopes at long periods in the upper mantle shows that the characteristic scale  $a=2000 \text{ km}$  is much larger than those at short periods of MU3 and ML1. Several measurements a priori suppose  $\kappa = 0.5$ ; however, most of measurements show  $\kappa < 0.5$  except L6. Measurements ML3 and MW1 propose the H-G type (see eq. (4)) corresponding to  $\kappa = 0$  for the lower/whole mantle. We note that Mancinelli et al. (2016b) proposed an alternative model of 3D-PSDF  $\propto m^{-2.6}$  in addition to ML3.

### 3.6.3 RTT with the phase screen approximation

When  $ak_c \gg 1$ , scattering mostly occurs within a narrow angle around the forward direction. At a large travel distance, the wavelet just after the onset is mostly composed of those waves. The phase screen approximation correctly calculates the phase



shift modulation. For the incidence of a plane wave into the  $z$  direction, the mutual coherence function (MCF) of the phase shift modulated waves for an increment  $\Delta z$  is given by

$$\Phi(k_c, r_\perp, \Delta z) = e^{-k_c^2(A(0)-A(r_\perp))\Delta z}. \quad (7a)$$

The longitudinal integral of the ACF is

$$A(r_\perp) = \int_{-\infty}^{\infty} R(\mathbf{x}_\perp, z) dz = \frac{1}{(2\pi)^2} \iint_{-\infty}^{\infty} P(\mathbf{m}_\perp, m_z = 0) e^{i\mathbf{m}_\perp \cdot \mathbf{x}_\perp} d\mathbf{m}_\perp, \quad (7b)$$

where  $\mathbf{x}_\perp$  is the transverse coordinate vector and  $r_\perp = |\mathbf{x}_\perp|$  (Sato et al., 2012, eq. 9.60). Taking the Fourier transform of MCF  $\Phi$  with respect to transverse coordinates, we have

$$\check{\Phi}(k_c, k_\perp, \Delta z) = \frac{1}{(2\pi)^2} \iint_{-\infty}^{\infty} \Phi(k_c, r_\perp, \Delta z) e^{i\mathbf{k}_\perp \cdot \mathbf{x}_\perp} d\mathbf{x}_\perp \xrightarrow{\Delta z \rightarrow 0} \delta(\mathbf{k}_\perp). \quad (7c)$$

Since  $\iint_{-\infty}^{\infty} \check{\Phi}(k_c, k_\perp, \Delta z) d\mathbf{k}_\perp = 1$ , interpreting  $\check{\Phi}(k_c, k_\perp, \Delta z)$  as the probability of ray bending angle  $\psi = \tan^{-1} \frac{k_\perp}{k_c}$  per  
 10 increment  $\Delta z = V_0 \Delta t$ , we can stochastically synthesize the intensity by using the Monte Carlo simulation (e.g Williamson, 1972; Takahashi et al., 2008; Saito et al., 2008). As a simple example, Figure 7 (b) schematically illustrates the flowchart of the RTT with the phase screen approximation for the isotropic radiation from a point source in uniform random media. Different from the Born approximation, ray bending occurs at every time step. The intensity Green function can be obtained in the same manner as the RTT with the Born approximation. This approximation well synthesizes the intensity time trace having a  
 15 delayed peak from the onset and a decaying tail at large travel distances. The Markov approximation is known as a stochastic extension of the phase screen method for the two-frequency mutual coherence function (e.g. Saito et al., 2002). If we focus on the intensity time trace around the peak arrival, the Markov approximation and the RTT with the phase screen approximation show good coincidence between them (Sato and Emoto, 2018). We note that this approximation can not synthesize the coda intensity since wide angle scattering is neglected.

20 When this approximation is used,  $k_c \gg a^{-1}$  is a priori supposed. Most of this type of measurements read the peak delay and the envelope width of each seismogram envelope. There is a merit that the peak delay measurement is rather insensitive to intrinsic absorption. Narrow angle scattering is mostly produced by the PSDF in low wavenumbers compared with  $k_c$ . For a given wavenumber range  $(k_l, k_u)$  (gray) in Figure 6, each PSDF curve using this method in Figure 3 is drawn by a dotted line for  $(0, k_l)$  and a solid line for  $(k_l, k_u)$  as the bottom line of Figure 6. In the NE Japan,  $\kappa$  value beneath a volcano LS2 is smaller  
 25 than those in the fore-arc side L12 and L13.

### 3.7 Characteristics of von Kármán parameters

#### 3.7.1 All the data

Some measurements a priori assumed  $\kappa = 0.5$ ; however, most of measurements report  $\kappa < 0.5$ . In the mantle,  $\kappa$  is very small close to zero and H-G type is also proposed. The RMS fractional fluctuation  $\varepsilon$  is of the order of 0.1 for rock samples and well

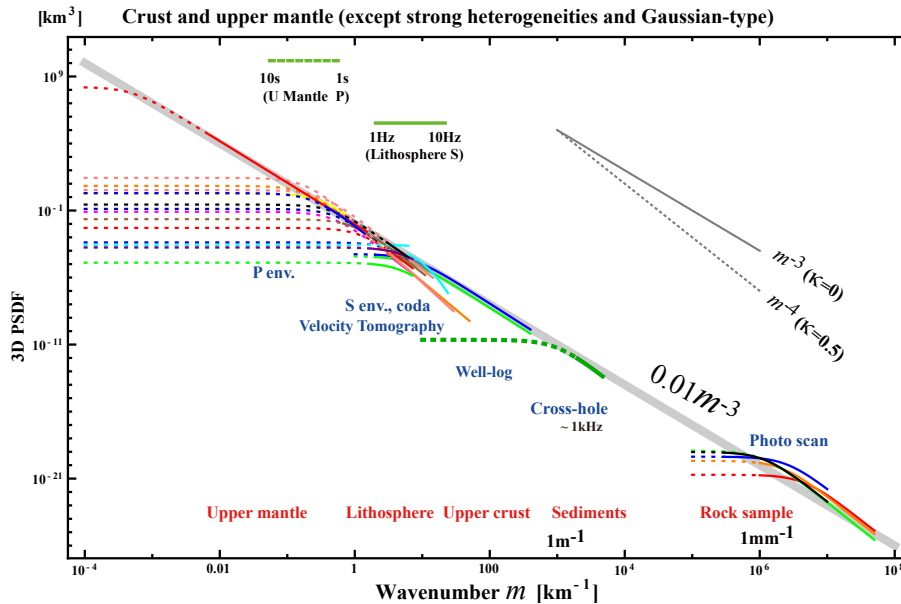


**Figure 8.** 3D PSDF vs. wavenumber for the crust and upper mantle. Data of Gaussian-type, anisotropic type, strong heterogeneities, the lower mantle, and the whole mantle are excluded. The light gray straight line visually well fits to the all spectral envelopes.

log data and of the order from 0.01 to 0.1 in the lithosphere and the upper mantle. Large values are measured in the shallow crust L16 and beneath a volcano LS3, however, smaller values are reported for the lower mantle. The characteristic scale  $a$  varies a lot depending on measurements. The corner wavenumber  $a^{-1}$  is not clearly seen in PSDFs of acoustic well logs. Some measurements report anisotropy: W3 of well-logs, L1 of velocity tomography in the shallow crust and LS5 in the subducting oceanic slab. Plotting PSDFs against wavenumber is more informative for understanding the random heterogeneity compared with listing statistical parameter numerals. Figure 4 (b) shows the plot of 3D PSDF vs. wavenumber for all the data covering a wide wavenumber range  $10^{-4} \sim 10^8 \text{ km}^{-1}$ . We recognize that PSDFs supposing Gaussian type shows very different behavior and those in the lower mantle take smaller values.

### 3.7.2 All the data in the lithosphere and the upper mantle except strong heterogeneity data

Eliminating strong heterogeneity data LS1~LS4, data supposing Gaussian type LA1~LA3, and the lower mantle and whole mantle data ML1~ML4 and MW1~MW2, we plot the rest of data for the crust and upper mantle in Figure 8. We draw a power-law decay curve  $0.01m^{-3} \text{ km}^3$  (gray) visually fitting to the envelope of all the PSDFs for a very wide range of wavenumbers  $10^{-3} \sim 10^8 \text{ km}^{-1}$ . This curve looks as if an extension of MU2 in the upper mantle (Mancinelli et al., 2016a) into higher wavenumbers of the shallow crust. The estimated power-law spectral envelope reflects the following facts: most of  $\varepsilon$  values are of the order of  $0.01 \sim 0.1$ , most of  $\kappa$  values are less than or equal to 0.5 and many of them are close to 0, and the high wavenumber end of the power-law decay branch of each PSDF is not far from each corner wavenumber.



#### 4 Discussions

It will be necessary for us to measure the small-scale randomness of sedimentary rock samples. More measurements are necessary in the wavenumber range  $10^3 \sim 10^5 \text{ km}^{-1}$  since there are few measurements. In most of PSDF measurements, each power-law decay branch is short since the Born approximation senses the spectrum up to twice the wavenumber. It will be necessary to measure how each power-law decay branch varies with wavenumber increasing.

The characteristic length  $a$  seems to increase as the wavenumber of a wavelet decreases or as the dimension of measurement system becomes large. It reminds us that the characteristic scale of the slip distribution increases with increasing source dimension as Mai and Beroza (2002) analyzed finite-fault source inversion results (see their Figure 12). It will be necessary to estimate the corner  $a^{-1}$  by using a measurement with a wide wavenumber-range covering sufficiently large enough the both sides of the corner. The flat part, the low-wavenumber side of each PSDF drawn by a dotted line in Figures is also important as the cause of narrow angle scattering.

The existence of the power-law decay spectral envelope seems to suggest that the random heterogeneities of the earth medium have a very broad spectrum. In observation, we may take the power-law spectral envelope as a reference curve for studying the regional differences especially in the power-law decay part of the PSDF.

There are a few measurements of anisotropy of randomness observed in the shallow crust and the oceanic lithosphere, which may reflect the effect of gravity. It will be interesting to study how a wavelet collapses after propagating through anisotropic random media (e.g. Margerin, 2006).

In section 3.6, we mentioned that the Born approximation is inapplicable and the phase screen approximation is useful when the phase shift becomes large as the wavenumber increases. In order to avoid the difficulty, taking the center wavenumber of a wavelet as a reference, Sato and Emoto (2018) divided the PSDF into two components (see also Sato, 2016; Sato and Emoto, 2017). They proposed to use the Born and phase screen approximations to the short-scale (high-wavenumber) and long-scale (low-wavenumber) components, respectively, in the RTT. Figure 9 illustrates the flowchart of their Monte Carlo simulation. Their spectrum division method looks an implementation of the distorted-wave Born approximation in the RTT since it describes wide angle scattering for the incidence of the phase shift modulated wave. They successfully synthesized intensity time traces that well explain FD simulation results for the case of  $ak_c = 23.6$  and  $\varepsilon^2 a^2 k_c^2 = 1.39$ .

However, some papers numerically show that the RTT with the Born approximation works well in some cases over the above limitation. Przybilla et al. (2006) synthesizes vector-wave intensity that well fits to that of the FD simulation in 2D even for S-waves of  $ak_c=58$  and  $\varepsilon^2 a^2 k_c^2 = 8.4$  (see their Table 1) if the wandering effect is convolved as a result of the travel time fluctuation. Emoto and Sato (2018) shows that the synthesized scalar intensity by the RTT with the Born approximation well fits to that of the FD simulation in 3D even for the case of  $ak_c = 23.6$  and  $\varepsilon^2 a^2 k_c^2 = 1.39$  when the wandering effect is convolved. If the earth heterogeneity is represented by a power-law decay power spectrum for such a wide wavenumber range, which means that the corner wavenumber is very low, we should carefully examine the applicability of the Born approximation in the RTT.

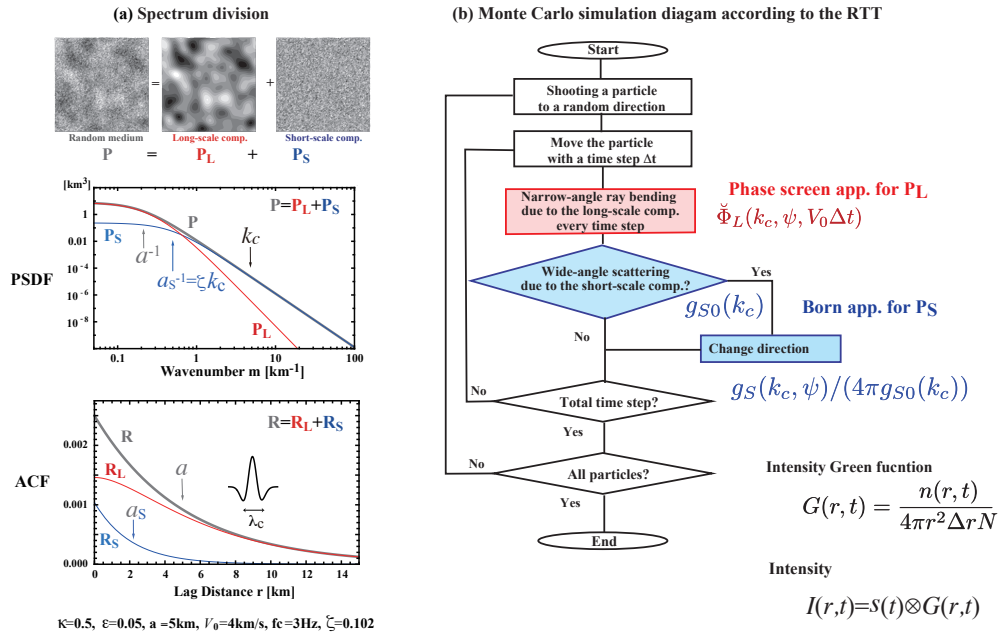


**Figure 9.** Spectrum division method. (a) Division of  $P$  into two components,  $P_S$  and  $P_L$ , with respect to the center wavenumber of a wavelet  $k_c$  as a reference, where  $\zeta$  is a tuning parameter. (b) Flow-chart of the Monte Carlo simulation according to the RTT with the spectrum division method. Modified from Sato and Emoto (2018).

The power-law decay spectral envelope reminds us of the observed fractal nature of various kinds of surface topographies: Sayles and Thomas (1978a, b) show  $1D\text{-PSDF} \propto m^{-2}$  for wavelengths  $10^{-6} \sim 10^3$  km although the power exponent varies from  $-1.07$  to  $-3.03$  for small segments; Brown and Scholz (1985) show  $1D\text{-PSDF} \propto m^{-1.64 \sim -3.36}$  for the wavenumber range  $10^{-6} \sim 0.1 \mu^{-1}$  especially for the topography of natural rock surfaces and faults. We also note that the PSDF of the refractive index fluctuation of air obeys the Kolmogorov spectrum:  $3D\text{-PSDF} \propto m^{-11/3}$ , where  $\kappa = 1/3$ . This spectrum is physically produced by the cascade in the turbulent flow of low viscosity air: the large eddies breaks up originating smaller eddies dissipating energy by viscosity. However, it is difficult to apply this model to the mantle since the viscosity of mantle fluid is thought to be high.

For igneous rocks such as granite, there are variations in composition of minerals and grain sizes, which depend on a variety of slow crystallization differentiations of basaltic magma. Random variations of acoustic well-log profiles reflect the complex sedimentation process during the geological history. Volcanism produces more heterogeneous structures composed of pyroclastic material and lava. For random heterogeneities in the mantle, we imagine complex mantle flow. Mancinelli et al. (2016a) referred to a marble cake mantle model (Allègre and Turcotte, 1986) containing heterogeneity mostly composed of basalt and harzburgite in many scales in the upper mantle in order to explain the power-law spectrum. Ricard et al. (2014) speculated that most of frequency-independent attenuation would not be caused by intrinsic absorption but scattering if the



power-law spectrum were present. If we accept the power-law decay spectrum even at high wavenumbers and in the crust, we will have to study what kinds of geophysical mechanisms created such random medium spectra in different scales and in different portions of the solid earth.

## 5 Conclusions

5 Recent seismological observations focusing on the collapse of an impulsive wavelet revealed the existence of small-scale random heterogeneities in the earth medium. The radiative transfer theory has been often used for the study of the propagation and scattering of wavelet intensities, the MS amplitude envelopes. For the statistical characterization of the PSDF of random velocity inhomogeneities in a 3D space, we have used von Kármán type with three parameters: the RMS fractional velocity fluctuation  $\varepsilon$ , the characteristic length  $a$ , and the order  $\kappa$  of the modified Bessel function of the second kind, which leads to the  
10 power-law decay of PSDF  $\propto m^{-2\kappa-3}$  at wavenumber  $m$  higher than the corner at  $a^{-1}$ . We have compiled reported statistical parameters of the lithosphere and the mantle based on various types of measurements for a wide range of wavenumbers: photo scan data of rock samples, acoustic well log data, and envelope analyses of cross-hole experiment seismograms, regional seismograms and tele-seismic waves based on the RTT. Reported  $\kappa$  values are distributed between 0 and 0.5 (PSDF  $\propto m^{-3\sim-4}$ ), where many of them are close to 0 (PSDF  $\propto m^{-3}$ ). Reported  $\varepsilon$  values are of the order of 0.01~0.1 in the crust and the upper  
15 mantle and smaller values in the lower mantle. Reported  $a$  values distribute very widely, however, each one seems to be restricted by the dimension of the measurement system or the sample length. In order to grasp the spectral characteristics, eliminating strong heterogeneity data and the lower mantle data, we have plotted all the reported PSDFs in the crust and the upper mantle against wavenumber  $m$  for a wide range  $10^{-3} \sim 10^8 \text{ km}^{-1}$ . We find that the envelope of those PSDFs is well approximated by a power-law decay curve  $0.01 m^{-3} \text{ km}^3$ . Multiple plots of PSDFs and the power-law decay spectral envelope  
20 obtained require us to do the followings: In theory, it will be necessary to examine whether the Born approximation is reliable or not if the wavenumber increases much larger than the corner; in observation, we will have to examine more carefully the behavior of each PSDF on both sides of the corner. If we accept the power-law decay spectral envelope, it suggests that the earth medium randomness has a broad spectrum. We may consider the obtained power-law decay spectral envelope as a reference for studying the regional differences. It is interesting to study what kinds of geophysical processes created the power-law  
25 spectral envelope in different scales and in different portions of the solid earth medium.

*Competing interests.* The author declares that he has no conflict of interest.

*Acknowledgements.* This paper is a part of the Beno Gutenberg medal lecture at the 2018 EGU assembly held in Vienna. The author is grateful to the seismology section of EGU for giving him an opportunity for reviewing measurements of random heterogeneities of the solid earth and various theoretical approaches. The author expresses sincere thanks to his colleagues and ex-graduate students who enthusiastically  
30 collaborated with him in studying seismic wave scattering in random media.



## References

- Aki, K.: Scattering of P waves under the Montana LASA, *J. Geophys. Res.*, 78, 1334–1346, <https://doi.org/10.1029/JB078i008p01334>, 1973.
- Aki, K. and Chouet, B.: Origin of coda waves: Source, attenuation and scattering effects, *J. Geophys. Res.*, 80, 3322–3342, 1975.
- Allègre, C. J. and Turcotte, D. L.: Implications of a two-component marble-cake mantle, *Nature*, 323, 123, 1986.
- 5 Bentham, H., Rost, S., and Thorne, M.: Fine-scale structure of the mid-mantle characterised by global stacks of PP precursors, *Earth and Planetary Science Letters*, 472, 164–173, 2017.
- Brown, S. R. and Scholz, C. H.: Broad bandwidth study of the topography of natural rock surfaces, *Journal of Geophysical Research: Solid Earth*, 90, 12 575–12 582, 1985.
- Calvet, M. and Margerin, L.: Lapse-Time Dependence of Coda Q: Anisotropic Multiple-Scattering Models and Application to the Pyrenees,  
10 *Bulletin of the Seismological Society of America*, 103, 1993–2010, 2013.
- Capon, J.: Characterization of crust and upper mantle structure under LASA as a random medium, *Bull. Seism. Soc. Am.*, 64, 235–266, 1974.
- Carcolé, E. and Sato, H.: Spatial distribution of scattering loss and intrinsic absorption of short-period S waves in the lithosphere of Japan on the basis of the Multiple Lapse Time Window Analysis of Hi-net data, *Geophys. J. Int.*, 180, 268–290,  
15 <https://doi.org/10.1111/j.1365-246X.2009.04394.x>, 2010.
- Chernov, L. A.: *Wave Propagation in a Random Medium* (Engl. trans. by R. A. Silverman), McGraw-Hill, New York, 1960.
- Chevrot, S., Montagner, J., and Snieder, R.: The spectrum of tomographic earth models, *Geophysical Journal International*, 133, 783–788, 1998.
- Cormier, V. F.: Anisotropy of heterogeneity scale lengths in the lower mantle from PKIKP precursors, *Geophysical Journal International*,  
20 136, 373–384, 1999.
- da Silva, J. J. A., Poliannikov, O. V., Fehler, M., and Turpening, R.: Modeling scattering and intrinsic attenuation of cross-well seismic data in the Michigan Basin, *Geophysics*, 83, WC15–WC27, 2018.
- Emoto, K. and Sato, H.: Statistical characteristics of scattered waves in 3-D random media: Comparison of the finite difference simulation and statistical methods, Preprint, Submitted to *Geophys. J. Int.*, 2018.
- 25 Emoto, K., Saito, T., and Shiomi, K.: Statistical parameters of random heterogeneity estimated by analysing coda waves based on finite difference method, *Geophysical Journal International*, 211, 1575–1584, 2017.
- Eulenfeld, T. and Wegler, U.: Crustal intrinsic and scattering attenuation of high-frequency shear waves in the contiguous United States, *Journal of Geophysical Research: Solid Earth*, 122, 4676–4690, 2017.
- Flatté, S. M. and Wu, R. S.: Small-scale structure in the lithosphere and asthenosphere deduced from arrival time and amplitude fluctuations  
30 at NORSAR, *J. Geophys. Res.*, 93, 6601–6614, <https://doi.org/10.1029/JB093iB06p06601>, 1988.
- Fukushima, Y., Nishizawa, H., Sato, H., and Ohtake, M.: Laboratory study on scattering characteristics of shear waves in rock samples, *Bull. Seism. Soc. Am.*, 93, 253–263, <https://doi.org/10.1785/0120020074>, 2003.
- Furumura, T. and Kennett, B. L. N.: Subduction zone guided waves and the heterogeneity structure of the subducted plate: Intensity anomalies in northern Japan, *J. Geophys. Res.*, 110, B10302, <https://doi.org/10.1029/2004JB003486>, 2005.
- 35 Gaebler, P. J., Sens-Schönfelder, C., and Korn, M.: The influence of crustal scattering on translational and rotational motions in regional and teleseismic coda waves, *Geophysical Journal International*, 201, 355–371, 2015.



- Gusev, A. A. and Abubakirov, I. R.: Monte-Carlo simulation of record envelope of a near earthquake, *Phys. Earth Planet. Inter.*, 49, 30–36, [https://doi.org/10.1016/0031-9201\(87\)90130-0](https://doi.org/10.1016/0031-9201(87)90130-0), 1987.
- Heney, L. G. and Greenstein, J. L.: Diffuse radiation in the galaxy, *The Astrophysical Journal*, 93, 70–83, 1941.
- Hock, S., Korn, M., Ritter, J. R. R., and Rothert, E.: Mapping random lithospheric heterogeneities in northern and central Europe, *Geophys. J. Int.*, 157, 251–264, <https://doi.org/10.1111/j.1365-246X.2004.02191.x>, 2004.
- Holliger, K.: Upper-crustal seismic velocity heterogeneity as derived from a variety of P-wave sonic logs, *Geophys. J. Int.*, 125, 813–829, <https://doi.org/10.1111/j.1365-246X.1996.tb06025.x>, 1996.
- Hoshiya, M., Sato, H., and Fehler, M.: Numerical basis of the separation of scattering and intrinsic absorption from full seismogram envelope - A Monte-Carlo simulation of multiple isotropic scattering, *Pa. Meteorol. Geophys., Meteorol. Res. Inst.*, 42, 65–91, 1991.
- Jing, Y., Zeng, Y., and Lin, G.: High-Frequency Seismogram Envelope Inversion Using a Multiple Nonisotropic Scattering Model: Application to Aftershocks of the 2008 Wells Earthquake, *Bulletin of the Seismological Society of America*, 104, 823–839, 2014.
- Kobayashi, M., Takemura, S., and Yoshimoto, K.: Frequency and distance changes in the apparent P-wave radiation pattern: effects of seismic wave scattering in the crust inferred from dense seismic observations and numerical simulations, *Geophysical Journal International*, 202, 1895–1907, 2015.
- Korn, M.: Determination of site-dependent scattering Q from P-wave coda analysis with an energy-flux model, *Geophys. J. Int.*, 113, 54–72, <https://doi.org/10.1111/j.1365-246X.1993.tb02528.x>, 1993.
- Kubanza, M., Nishimura, T., and Sato, H.: Evaluation of strength of heterogeneity in the lithosphere from peak amplitude analyses of teleseismic short-period vector P waves, *Geophys. J. Int.*, 171, 390–398, <https://doi.org/10.1111/j.1365-246X.2007.03544.x>, 2007.
- Landau, L. and Lifshitz, E.: *Quantum Mechanics* (3rd Ed., Engl. trans. by J. B. Sykes and J. S. Bell), Butterworth-Heinemann, 2003.
- Mai, P. M. and Beroza, G. C.: A spatial random field model to characterize complexity in earthquake slip, *Journal of Geophysical Research: Solid Earth*, 107, ESE–10, 2002.
- Mancinelli, N., Shearer, P., and Liu, Q.: Constraints on the heterogeneity spectrum of Earth's upper mantle, *Journal of Geophysical Research: Solid Earth*, 121, 3703–3721, 2016a.
- Mancinelli, N., Shearer, P., and Thomas, C.: On the frequency dependence and spatial coherence of PKP precursor amplitudes, *Journal of Geophysical Research: Solid Earth*, 121, 1873–1889, 2016b.
- Margerin, L.: Introduction to radiative transfer of seismic waves, in "Seismic Earth: Array Analysis of Broadband Seismograms" (Eds. A. Levander and G. Nolet), vol. 157, pp. 229–252, *Geophysical Monograph-American Geophysical Union*, 2005.
- Margerin, L.: Attenuation, transport and diffusion of scalar waves in textured random media, *Tectonophysics*, 416, 229–244, 2006.
- Margerin, L. and Nolet, G.: Multiple scattering of high-frequency seismic waves in the deep Earth: PKP precursor analysis and inversion for mantle granularity, *J. Geophys. Res.*, 108, 2514, <https://doi.org/10.1029/2003JB002455>, 2003.
- Margerin, L., Campillo, M., and Tiggelen, B. V.: Monte Carlo simulation of multiple scattering of elastic waves, *J. Geophys. Res.*, 105, 7873–7893, <https://doi.org/10.1029/1999JB900359>, 2000.
- Meschede, M. and Romanowicz, B.: Lateral heterogeneity scales in regional and global upper mantle shear velocity models, *Geophysical Journal International*, 200, 1076–1093, 2015.
- Morioka, H., Kumagai, H., and Maeda, T.: Theoretical basis of the amplitude source location method for volcano-seismic signals, *Journal of Geophysical Research: Solid Earth*, 2017.
- Nakata, N. and Beroza, G. C.: Stochastic characterization of mesoscale seismic velocity heterogeneity in Long Beach, California, *Geophysical Journal International*, 203, 2049–2054, 2015.



- Petukhin, A. and Gusev, A.: The duration-distance relationship and average envelope shapes of small Kamchatka earthquakes, *Pure Appl. Geophys.*, 160, 1717–1743, <https://doi.org/10.1007/s00024-003-2373-5>, 2003.
- Powell, C. A. and Meltzer, A. S.: Scattering of P-waves beneath SCARLET in southern California, *Geophys. Res. Lett.*, 11, 481–484, <https://doi.org/10.1029/GL011i005p00481>, 1984.
- 5 Przybilla, J., Korn, M., and Wegler, U.: Radiative transfer of elastic waves versus finite difference simulations in two-dimensional random media, *J. Geophys. Res.*, 111, <https://doi.org/10.1029/2005JB003952>, 2006.
- Przybilla, J., Wegler, U., and Korn, M.: Estimation of crustal scattering parameters with elastic radiative transfer theory, *Geophys. J. Int.*, 178, 1105–1111, <https://doi.org/10.1111/j.1365-246X.2009.04204.x>, 2009.
- Ricard, Y., Durand, S., Montagner, J.-P., and Chambat, F.: Is there seismic attenuation in the mantle?, *Earth and Planetary Science Letters*, 10 388, 257–264, 2014.
- Rost, S., Thorne, M. S., and Garnero, E. J.: Imaging global seismic phase arrivals by stacking array processed short-period data, *Seismological Research Letters*, 77, 697–707, 2006.
- Rotherth, E. and Ritter, J. R.: Small-scale heterogeneities below the Gräfenberg array, Germany from seismic wavefield fluctuations of Hindu Kush events, *Geophysical Journal International*, 140, 175–184, 2000.
- 15 Rytov, S. M., Kravstov, Y. A., and Tatarskii, V. I.: *Principles of Statistical Radiophysics (Vol. 4) Wave Propagation Through Random Media*, Springer-Verlag, Berlin, 1989.
- Saito, T., Sato, H., and Ohtake, M.: Envelope broadening of spherically outgoing waves in three-dimensional random media having power-law spectra, *J. Geophys. Res.*, 107, <https://doi.org/10.1029/2001JB000264>, 2002.
- Saito, T., Sato, H., Ohtake, M., and Obara, K.: Unified explanation of envelope broadening and maximum-amplitude decay of high-frequency 20 seismograms based on the envelope simulation using the Markov approximation: Forearc side of the volcanic front in northeastern Honshu, Japan, *J. Geophys. Res.*, 110, <https://doi.org/10.1029/2004JB003225>, 2005.
- Saito, T., Sato, H., and Takahashi, T.: Direct simulation methods for scalar-wave envelopes in two-dimensional layered random media based on the small-angle scattering approximation, *Commun. Comput. Phys.*, 3, 63–84, 2008.
- Sanborn, C. J., Cormier, V. F., and Fitzpatrick, M.: Combined effects of deterministic and statistical structure on high-frequency regional 25 seismograms, *Geophysical Journal International*, p. ggx219, 2017.
- Sato, H.: Energy propagation including scattering effects: Single isotropic scattering approximation, *J. Phys. Earth*, 25, 27–41, 1977a.
- Sato, H.: Attenuation and envelope formation of three-component seismograms of small local earthquakes in randomly inhomogeneous lithosphere, *J. Geophys. Res.*, 89, 1221–1241, <https://doi.org/10.1029/JB089iB02p01221>, 1984.
- Sato, H.: Broadening of seismogram envelopes in the randomly inhomogeneous lithosphere based on the parabolic approximation: South- 30 eastern Honshu, Japan, *J. Geophys. Res.*, 94, 17 735–17 747, <https://doi.org/10.1029/JB094iB12p17735>, 1989.
- Sato, H.: Envelope broadening and scattering attenuation of a scalar wavelet in random media having power-law spectra, *Geophysical Journal International*, 204, 386–398, <https://doi.org/doi:10.1093/gji/ggv442>, 2016.
- Sato, H. and Emoto, K.: Synthesis of a scalar wavelet intensity propagating through von Kármán-type random media: joint use of the radiative transfer equation with the Born approximation and the Markov approximation, *Geophysical Journal International*, 211, 512–527, 35 <https://doi.org/10.1093/gji/ggx318>, +<http://dx.doi.org/10.1093/gji/ggx318>, 2017.
- Sato, H. and Emoto, K.: Synthesis of a scalar wavelet intensity propagating through von Kármán-type random media: Radiative transfer theory using the Born and phase-screen approximations, *Geophysical Journal International*, 215, 909–923, 2018.
- Sato, H., Fehler, M. C., and Maeda, T.: *Seismic wave propagation and scattering in the heterogeneous earth: Second Edition*, Springer, 2012.



- Sayles, R. S. and Thomas, T. R.: Surface topography as a non-stationary random process, *Nature*, 271, 431, 1978a.
- Sayles, R. S. and Thomas, T. R.: Reply to "Topography of random surfaces, *Nature*, 273, 573, 1978b.
- Sens-Schönfelder, C., Margerin, L., and Campillo, M.: Laterally heterogeneous scattering explains Lg blockage in the Pyrenees, *J. Geophys. Res.*, 114, B07 309, <https://doi.org/10.1029/2008JB006107>, 2009.
- 5 Shearer, P. M. and Earle, P. S.: The global short-period wavefield modelled with a Monte Carlo seismic phonon method, *Geophys. J. Int.*, 158, 1103–1117, <https://doi.org/10.1111/j.1365-246X.2004.02378.x>, 2004.
- Shiomi, K., Sato, H., and Ohtake, M.: Broad-band power-law spectra of well-log data in Japan, *Geophys. J. Int.*, 130, 57–64, <https://doi.org/10.1111/j.1365-246X.1997.tb00987.x>, 1997.
- Sivaji, C., Nishizawa, O., Kitagawa, G., and Fukushima, Y.: A physical-model study of the statistics of seismic waveform fluctuations in  
10 random heterogeneous media, *Geophys. J. Int.*, 148, 575–595, <https://doi.org/10.1046/j.1365-246x.2002.01606.x>, 2002.
- Spetzler, J., Sivaji, C., Nishizawa, O., and Fukushima, Y.: A test of ray theory and scattering theory based on a laboratory experiment using ultrasonic waves and numerical simulation by finite-difference method, *Geophysical Journal International*, 148, 165–178, 2002.
- Takahashi, T., Sato, H., and Nishimura, T.: Recursive formula for the peak delay time with travel distance in von Karman type non-uniform random media on the basis of the Markov approximation, *Geophys. J. Int.*, 173, 534–545,  
15 <https://doi.org/10.1111/j.1365-246X.2008.03739.x>, 2008.
- Takahashi, T., Sato, H., Nishimura, T., and Obara, K.: Tomographic inversion of the peak delay times to reveal random velocity fluctuations in the lithosphere: method and application to northeastern Japan, *Geophys. J. Int.*, 178, 1437–1455, <https://doi.org/10.1111/j.1365-246X.2009.04227.x>, 2009.
- Takemura, S., Furumura, T., and Saito, T.: Distortion of the apparent S-wave radiation pattern in the high-frequency wavefield: Tottori-Ken  
20 Seibu, Japan, earthquake of 2000, *Geophys. J. Int.*, 178, 950–961, <https://doi.org/10.1111/j.1365-246X.2009.04210.x>, 2009.
- Wang, W. and Shearer, P.: Using direct and coda wave envelopes to resolve the scattering and intrinsic attenuation structure of Southern California, *Journal of Geophysical Research: Solid Earth*, 122, 7236–7251, 2017.
- Williamson, I. P.: Pulse broadening due to multiple scattering in the interstellar medium, *Mon. Not. R. Astron. Soc.*, 157, 55–71, 1972.
- Wu, R. S., Xu, Z., and Li, X. P.: Heterogeneity spectrum and scale-anisotropy in the upper crust revealed by the German Continental  
25 Deep-Drilling (KTB) holes, *Geophys. Res. Lett.*, 21, 911–914, <https://doi.org/10.1029/94GL00772>, 1994.
- Yoshimoto, K.: Monte-Carlo simulation of seismogram envelope in scattering media, *J. Geophys. Res.*, 105, 6153–6161, <https://doi.org/10.1029/1999JB900437>, 2000.
- Yoshimoto, K. and Jin, A.: Coda Energy Distribution and Attenuation, in: *Earth Heterogeneity and Scattering Effects on Seismic Waves*, edited by Sato, H. and Fehler, M. C., vol. 50 of *Advances in Geophysics (Series Ed. R. Dmowska)*, chap. 10, pp. 265–300, Academic  
30 Press, 2008.
- Yoshimoto, K., Sato, H., and Ohtake, M.: Three-component seismogram envelope synthesis in randomly inhomogeneous semi-infinite media based on the single scattering approximation, *Phys. Earth Planet. Inter.*, 104, 37–61, [https://doi.org/10.1016/S0031-9201\(97\)00061-7](https://doi.org/10.1016/S0031-9201(97)00061-7), 1997b.
- Zeng, Y.: Modeling of High-Frequency Seismic-Wave Scattering and Propagation Using Radiative Transfer Theory, *Bull. Seism. Soc. Am.*,  
35 107, 2948–2962, 2017.
- Zhang, B., Ni, S., Sun, D., Shen, Z., Jackson, J. M., and Wu, W.: Constraints on small-scale heterogeneity in the lowermost mantle from observations of near podal PcP precursors, *Earth and Planetary Science Letters*, 489, 267–276, 2018.



**Table 1.** Reported von Karmán parameters of rock samples and acoustic well logs.

Label	Rock type	ID-PSDF [km]	$\kappa$	$\varepsilon$	$a$ [km]	Wavenumber $m$ range [ $\text{km}^{-1}$ ]	Reference
<b>Photo scan of rock samples</b>							
R1	Westerly (fine) Granite, Vp, 1D	-	(0.5)	0.085	$0.22 \times 10^{-6}$	$(1 \sim 50) \times 10^6$	Sivaji et al. (2002)
R2	Oshima (medium) Granite, Vp, 1D	-	(0.5)	0.093	$0.46 \times 10^{-6}$	$(1 \sim 50) \times 10^6$	Sivaji et al. (2002)
R3	Inada (coarse) Granite, Vp, 1D	-	(0.5)	0.079	$0.92 \times 10^{-6}$	$(1 \sim 50) \times 10^6$	Sivaji et al. (2002)
R4	Oshima (medium) Granite, Vs, 1D	-	(0.5)	0.17	$0.39 \times 10^{-6}$	$(0.3 \sim 10) \times 10^6$	Fukushima et al. (2003)
R5	Tamura Gabbro, Vs, 1D	-	(0.5)	0.081	$0.84 \times 10^{-6}$	$(0.3 \sim 10) \times 10^6$	Fukushima et al. (2003)
<b>Acoustic well logs</b>							
W1	UM crust, YT-1, Japan, Vp, 1D	$3.3 \times 10^{-7} (\frac{2m}{10^4})^{-1.45}$	0.225	-	-	$(0.02 \sim 2) \times 10^3$	Shiomi et al. (1997)
W2	UM crust, IWT, Japan, Vp, 1D	$3.3 \times 10^{-7} (\frac{2m}{10^4})^{-1.09}$	0.045	-	-	$(0.01 \sim 2) \times 10^3$	Shiomi et al. (1997)
W3*	U crust, KTB, Germany, Vp, 1D	$\propto m^{-0.97}$	-0.015	-	$a_z > 1, a_h/a_z = 1.8$	$(0.001 \sim 0.5) \times 10^3$	Wu et al. (1994)
W4	U crust, KTB, Germany, Vp, 1D	$\propto m^{-1.2}$	0.10	0.048	0.16	$(0.002 \sim 0.4) \times 10^3$	Holliger (1996)
W5	U crust, Cajon Pass, Ca., Vp, 1D	$\propto m^{-1.22}$	0.11	0.067	0.14	$(0.002 \sim 0.4) \times 10^3$	Holliger (1996)



**Table 2.** Reported von Karman parameters of the lithosphere including the crust and the most-upper mantle.

Label	Region	Data & Method	3D-PSDF [km <sup>3</sup> ]	$\kappa$	$\varepsilon$	$\alpha$ [km]	$f$ range [Hz]	$m$ range [km <sup>-1</sup> ]	Reference
<b>Lithosphere (crust and upper-most mantle)</b>									
L1	UM crust, California	Vp Tomography, 3D	-	0.04	0.107	$a_z = 0.1$ $a_h = 0.51$ [0.0001]	$(1.2 \sim 2.8) \times 10^3$	1~80	Nakata and Beroza (2015)
L2	UM crust, Michigan	P&S env., Born 2D	-	(0.5)	[0.03]	0.01~0.05		$(2 \sim 4.7) \times 10^3$	da Silva et al. (2018)
L3	Lithos., Grafenberg	tele.-P env., FD	-	(0.5)	[0.03]		1.5~2.5	1.3~2.3	Rotherth and Ritter (2000)
L4	Crust, Grafenberg	P env., Born	-	(0.5)	0.029	0.27	4~8	3.6~7.2	Gaebler et al. (2015)
L5	Crust, Norway	P&S env., Born	-	0.2	0.059	4	2~10	3~15	Przybilla et al. (2009)
L6	Crust, Pyrenees	S coda, Born.	-	3	0.03	0.09	3~12	5.9~24	Calvet and Mangerin (2013)
L7	Crust, Pyrenees	P, S & Lg env., Born	-	(0.5)	0.021	0.77	2~4	3.6~7.2	Sens-Schönfelder et al. (2009)
L8	UM mantle, Pyrenees	P, S & Lg env., Born	-	(0.5)	0.02	2	2~4	3.6~7.2	Sens-Schönfelder et al. (2009)
L9	Crust, UM mantle, W. Japan	S-env., FD	-	(0.5)	0.05	3.1	0.063~0.5	0.1~0.7	Enoto et al. (2017)
L10	Crust, W. Japan.	SH amp., FD	-	(0.5)	0.07	3	2~8	3.6~14.4	Takemura et al. (2009)
L11	Crust, W. Japan	P env., FD	-	(0.5)	0.03	1	0.75~12	0.67~11	Kobayashi et al. (2015)
L12	Lithos., Fore-arc, NE Japan	S peak-delay, Markov	$0.008 m^{-4.2}$	0.6	0.042	[5]	2~32	3~50	Takahashi et al. (2009)
L13	Lithos., Fore-arc, NE Japan	S env., Markov	-	0.8	0.07	[5]	2~16	3~50	Saito et al. (2005)
L14	Crust, Lop Nor, China	Pg, Lg env., Born	-	0.3	0.04	0.2	1~4	1.8~7.2	Sauborn et al. (2017)
L15	MU mantle, Lop Nor, China	Pg, Lg env., Born	-	0.5	0.008	0.2	1~4	1.8~7.2	Sauborn et al. (2017)
L16	MU crust, California	P, S env., Born	-	(0.3)	0.4	0.05	2~4	3~6.2	Wang and Shearer (2017)
L17	L crust, California	P, S env., Born	-	(0.3)	0.05	2	2~4	3~6.2	Wang and Shearer (2017)
L18*	Lithos., Kamchatka	S env. broad, Born	$\propto m^{-3.85}$	0.425	-	-	0.5~16	0.9~29	Petukhin and Gusev (2003)
<b>Strong heterogeneities</b>									
LS1	Nikko, Japan	P & S coda, Born	-	(0.5)	0.07	0.5	8~16	14~29	Yoshimoto et al. (1997b)
LS2	Kurikoma volc. NE Japan	S peak-delay, Markov	$0.020 m^{-3.7}$	0.35	0.061	[5]	2~32	3~50	Takahashi et al. (2009)
LS3	Taal volc. Philippines	S-env., Born	-	(0.5)	0.2	0.05	5~10	13~25	Morioka et al. (2017)
LS4	Pyrenean hetero. body	P, S & Lg env., Born	-	(0.5)	0.072	0.77	2~4	3.6~7.2	Sens-Schönfelder et al. (2009)
LS5	Oceanic plate, Japan	S env., FD	-	(0.5)	0.02~0.03 [0.025]	$a_p=10$ , $a_t=0.5$	0.25~5	0.39~7.9	Furumura and Kennett (2005)
<b>Array analysis</b>									
LA1	Crust U mantle, Montana	tele.-P, Array	-	(Gaussian)	0.04	10	0.5	0.3~0.6	Aki (1973)
LA2	Crust, U mantle, Montana	tele.-P, Array	-	(Gaussian)	0.019	12	0.8	0.5~1	Capon (1974)
LA3	Crust, S. California	tele.-P, Array	-	(Gaussian)	0.0326	25	1	0.54~1.1	Powell and Meltzer (1984)
LA4	Crust, U mantle, Norway	tele.-P, Array	$\propto m^{-4} + W$ . noise	< 0.5	0.01~0.04	-	1~3	0.05~1.2	Flatté and Wu (1988)



**Table 3.** Reported von Karman parameters of the upper mantle and the lower mantle.

Label	Region	Data & Method	3D-PSDF [ $\text{km}^3$ ]	$\kappa$	$\epsilon$	$a$ [km]	$f$ range [Hz]	$m$ range [ $\text{km}^{-1}$ ]	Reference
<b>Upper mantle</b>									
MU1*	Upper mantle	$V_s$ Tomography, 2D	$\propto m^{-2 \sim -3} \text{km}^2$	0~0.5	–	> 500	–	0.006~0.01	Chevrot et al. (1998)
MU2	Upper mantle	P env., SEM, Born	–	0.05	0.1	2000	0.017~1	0.007~1.5	Mancinelli et al. (2016a)
MU3	Upper mantle	P env., Born	–	(0.5)	0.03~0.04 [0.035]	4	0.5~2	0.37~1.4	Shearer and Earle (2004)
<b>Lower mantle</b>									
ML1	Lower mantle	P env., Born	–	(0.5)	0.005	8	0.5~2	0.26~1	Shearer and Earle (2004)
ML2	ML mantle	PKIKP prec., FD	–	(Gaussian)	0.01	20	0.02~2	0.05~0.5	Cormier (1999)
ML3	W. Pacific, C/N Am.	PKP prec., Born	$2.5 \times 10^{-5} m^{-3}$	0, HG	0.002	$\geq 15$ [30]	0.5~4	0.2~4	Mancinelli et al. (2016b)
ML4	ML mantle	PeP env., Born, FD	–	(0.5)	0.002~0.01 [0.005]	8	0.8~1.5	0.39~0.72	Zhang et al. (2018)
<b>Whole mantle</b>									
MW1	Whole mantle	PKP prec., Born	$1.4 \times 10^{-5} m^{-3}$	0, HG	0.001~0.002 [0.0015]	$\geq 8$ [30]	0.4~2.5	0.2~1.3	Margerin and Nolet (2003)
MW2	Whole mantle	PP prec., Born	–	(0.5)	0.008~0.01 [0.009]	8	0.5~2.5	0.3~1.4	Benthien et al. (2017)